Enhanced laser cooling of rare-earth-ion-doped nanocrystalline powders

X. L. Ruan and M. Kaviany*

Department of Mechanical Engineering, University of Michigan, Ann Arbor, Michigan 48105, USA
(Received 17 August 2005; revised manuscript received 29 November 2005; published 21 April 2006)

The enhanced laser cooling performance of rare-earth-ion-doped nanocrystalline powders is predicted, compared to the bulk material, using $Yb^{3+}:Y_2O_3$ as the model material. This is achieved by enhancing the off-resonance, phonon-assisted absorption, which is proportional to the three factors considered in this paper: the dopant concentration, the pumping field energy, and the excitation coefficient. Using the energy transfer theory for concentration quenching, the optimum concentration corresponding to the maximum cooling power is found to be considerably larger than the currently used value, suggesting noticeable enhancement effects for laser cooling. The pumping field energy is enhanced in random nanopowders compared with bulk crystals under the same irradiation, due to the multiple scattering of photons. Photons are thus localized in the medium and do not propagate through, increasing the photon absorption of the pumping beam (and it is shown that the reabsorption of the fluorescence is negligible). Using molecular dynamics simulations, the phonon density of states (DOS) of the nanopowder is calculated, and found to have broadened modes, and extended small tails at low and high frequencies. The second-order electronic transition rate for the anti-Stokes luminescence is calculated using the Fermi golden rule, which includes the influence of this phonon DOS, and is shown to have enhancement effects on the laser cooling efficiency using nanopowders. It is finally concluded that these three enhancement mechanisms are essentially to increase the population of the three participating carriers (electron, photon, and phonon) in the interacting volume, and this also points out directions for enhancing laser cooling performance in bulk materials.

I. INTRODUCTION

The concept of laser cooling (optical refrigeration) of solids dates back to 1929, when Pringsheim recognized that thermal vibrational energy (phonon) might be removed by the anti-Stokes fluorescence, i.e., the photons emitted by an optical material have a mean energy higher than that of the absorbed photons.[1] This idea was initially believed to contradict the second law of thermodynamics. Predictions suggested that the cycle of excitation and fluorescence was reversible, and hence the optical cooling would be equivalent to the complete transformation of heat to work.[2,3] This issue was cleared by Landau by assigning entropy to radiation.[4] It was shown that the entropy of a radiation field is proportional to its frequency bandwidth and also to the solid angle through which it propagates. Since the incident laser light has a very small bandwidth and propagates in a well-defined direction, it has almost zero entropy. On the other hand, the fluorescence is relatively broadband and is propagating in all directions, and therefore, it has a comparatively larger entropy. In this way, the second law of thermodynamics is satisfied. A detailed, up-to-date analysis is given in the Appendix for reference.

In Fig. 1(a), the fundamental energy carriers involved in the laser cooling process are shown. A host crystal lattice, transparent to the pumping laser, has some of its atoms replaced by optically active ions (eg., Yb^{3+}), and thus, becomes slightly absorbing. The ion can be represented by an effective transition dipole moment, defined as a quantum mechanical spatial integral of the classical dipole moment $e_e\mathbf{r}$, i.e.,

$$\boldsymbol{\mu}_e = \int \psi_f^* e_e \mathbf{r} \psi_i \, d^3r, \tag{1}$$

where e_e is the electron charge, $\mathbf{r}$ is the position vector, and ψ_i and ψ_f are the initial and final state wave functions of the two level system. The electromagnetic field, which has a polarization vector $\mathbf{e}_\alpha$, may interact with the ion if the coupling factor $\mathbf{e}_\alpha \cdot \boldsymbol{\mu}_e$ is nonzero (i.e., they are not orthogonal). Shown in Fig. 1(b) is the principle of the photon-electron-phonon interactions that result in the cooling effect in the solid. When the medium is irradiated by laser light with a frequency $\omega_{ph,i}$ that is below the resonance frequency $\omega_{e,g}$ for the energy gap (10,250 cm^{-1} for Yb^{3+} ion in Y_2O_3), the electron may still be excited by absorbing a photon from the pumping field and a phonon with a frequency ω_p from the host, such that $\omega_{ph,i}+\omega_p=\omega_{e,g}$. The electron then decays by emitting a photon with a frequency $\omega_{ph,e}$ and, possibly, phonons. If the average emitted photon frequency $\bar{\omega}_{ph,e}$ is larger than $\omega_{ph,i}$, the medium loses thermal energy and is cooled.

Many attempts have been made to realize radiative refrigeration experimentally, and the associated theoretical interpretations have been discussed. The earliest experiment was performed by Kushida and Geusic on Nd: YAG.[5] Reduced heating other than net cooling was observed, which was conjectured to be a result of the impurities in the crystal and multiphonon decay across the optical transition. Later Djeu and Whitney laser cooled low-pressure CO_2 by 1 K from 600 K by using a CO_2 laser for pumping.[6] As late as 1995, Epstein *et al.* reported the first successful experiment of laser cooling in solids.[7] A local temperature decrease in a Yb-doped glass was detected by a photothermal deflection tech-
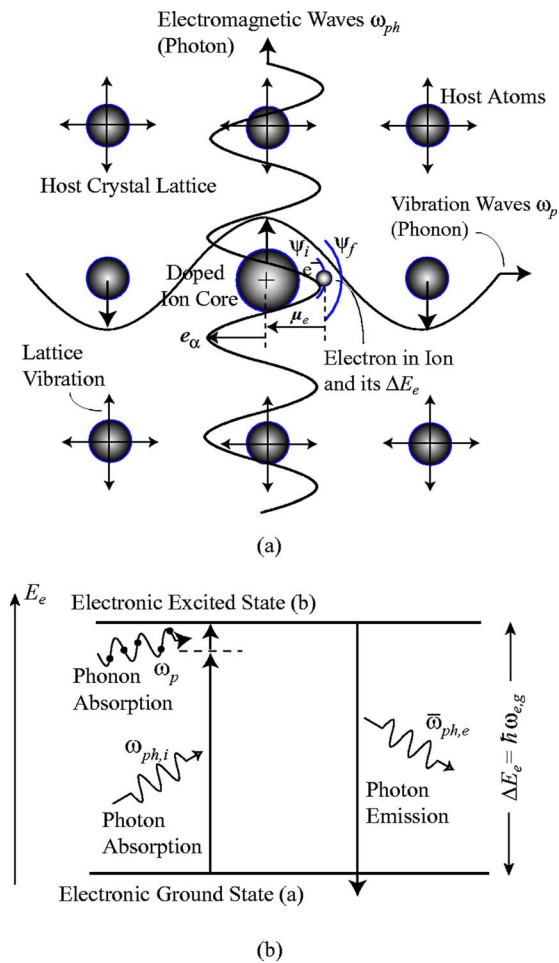
FIG. 1. (Color online) (a) Three fundamental energy carriers in rare-earth ion doped solids irradiated by laser light: photons from the pumping fields, phonons from the host crystal, and electrons of the doped ions. (b) Principles of laser cooling in a rare-earth ion doped crystal. The electron is excited by absorbing a photon and one or more lattice phonons, and then decays by emitting a higher energy photon.

nique. The achieved cooling efficiency η_c, defined as the ratio between the net cooling power and the absorbed power, was about 2%. Since then, various Yb or Tm doped glasses and crystals have been cooled,[8–17] among which the best performance to date is 92 K below room temperature.[17]

In these experiments, the pumping wavelength needs to be tuned far to the red side of the absorption resonance, since it must be longer than the mean emission wavelength to achieve cooling. As a result, the laser cooling performance is intrinsically limited by the very low absorption of the pumping photons. Here, we will theoretically explore the possible enhancement of the absorption by using nanopowders. A micrograph of the nanopowder[18] is shown in Fig. 2.

We will focus on the enhanced laser cooling of $Yb^{3+}:Y_2O_3$ nanopowder, and compare the predictions to those for bulk crystals. To start, we derive an expression for the total net cooling power in terms of various limiting factors, in order to provide guidelines for cooling power enhancement. It is found that the off-resonance, phonon-assisted absorption needs to be enhanced, which can be
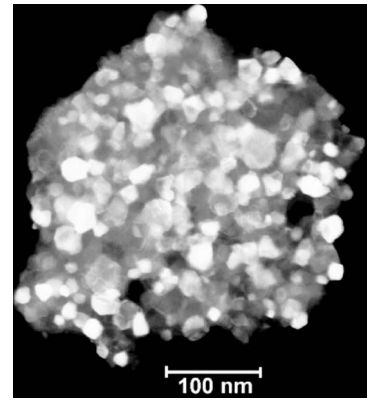

FIG. 2. A micrograph of an ion-doped nanopowder (Ref. 18).

achieved by increasing the number of absorbers, the pumping field energy, and the excitation coefficient. Nanopowders are then proposed to have all these features for the enhanced performance. Using the concentration quenching theory of energy transfer, the optimum concentration is introduced and found to be larger than the currently used value, suggesting noticeable enhancement effects for laser cooling. The pumping field energy is enhanced in random nanopowders than bulk crystals under the same irradiation, due to the multiple scattering of photons in random nanopowders. Using molecular dynamics simulations, the phonon density of states (DOS) of Y_2O_3 nanoparticles is calculated, and found to have broadened modes, and extended tails at low and high frequencies. The second-order, electronic transition rate for the anti-Stokes luminescence is calculated using the Fermi golden rule, which includes the influence of this phonon DOS, and is shown to have enhancement effects on the laser cooling efficiency using nanopowders. Finally, it is concluded that these three enhancement mechanisms correspond to an increase in the population of the three carriers (electron, photon, and phonon) in the interacting volume, respectively.

II. LIMITING FACTORS FOR LASER COOLING PERFORMANCE

In Fig. 3, a steady state energy diagram is shown for the laser cooling of nanopowders. The energy entering the control volume is the laser irradiation power $Q_{ph,i}$, and those leaving the control volume are the elastically scattered power $Q_{ph,s}$ and the fluorescence emission power $Q_{ph,f}$. The net
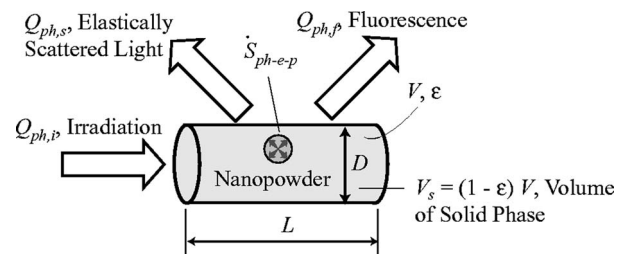

FIG. 3. The energy diagram for the laser cooling of a nanopowder. The external thermal load is not shown.

cooling power $\dot{S}_{ph\text{-}e\text{-}p}$ is given by $Q_{ph,i} - Q_{ph,s} - Q_{ph,f}$, and is balanced by some kind of external thermal load (for example, thermal radiation[11]), which is not shown in Fig. 3, since it is not the focus of this work. To minimize the fluorescence reabsorption, the sample is made into a very thin fiber-type geometry, as used by Gosnell in Ref. 11, where the length L is similar to 7 mm, and the diameter D is around 170 μm. The volume of the medium is V and the porosity is ϵ. The carrier interactions and energy conversions only take place in the volume of the solid phase, which is $V_s = (1 - \epsilon)V$. However, the presence of nanopores is important in that they affect the photon transport and the phonon DOS, as will be seen in later sections.

In order to relate the absorbed and emitted power, the population dynamics of the ground and excited electronic states need to be established. Although the rate equation is not suitable for describing atoms with any correlations between them (such as in cooperative interactions or other interatomic couplings), it is correct to describe the population dynamics of statistically independent atoms. In the nanoparticles studied, cooperative effects are negligible.[19] Hence, the rate equation for the two-level system shown in Fig. 1(b) is

$$\frac{dn_b}{dt} = -\dot{\gamma}_{e,d} n_b + \dot{\gamma}_{e,a} n_a + (1 - \eta_e) \dot{\gamma}_{e,r} n_b, \quad (2)$$

where n_b and n_a are the populations of the excited and ground states, respectively. Here, the intrinsic decay rate $\dot{\gamma}_{e,d}$ is the sum of the intrinsic radiative decay (includes the spontaneous and stimulated emissions) rate $\dot{\gamma}_{e,r}$ and the intrinsic nonradiative decay rate $\dot{\gamma}_{e,nr}$. The rate $\dot{\gamma}_{e,a}$ is the absorption (or excitation) rate. The last term in Eq. (2) accounts for the reabsorption effect, and η_e is the probability of a fluorescence photon to escape out of the medium without any reabsorption, or the so-called escape efficiency.[20] The intrinsic quantum efficiency is defined as

$$\eta_{e\text{-}ph} = \frac{\dot{\gamma}_{e,r}}{\dot{\gamma}_{e,d}} = \frac{\dot{\gamma}_{e,r}}{\dot{\gamma}_{e,r} + \dot{\gamma}_{e,nr}}. \quad (3)$$

In Eq. (2), the reabsorption term can be combined into the decay term, and the rate equation becomes

$$\frac{dn_b}{dt} = -[\dot{\gamma}_{e,r} + \dot{\gamma}_{e,nr} - (1 - \eta_e) \dot{\gamma}_{e,r}] n_b + \dot{\gamma}_{e,a} n_a n_b$$

$$= -(\eta_e \dot{\gamma}_{e,r} + \dot{\gamma}_{e,nr}) n_b + \dot{\gamma}_{e,a} n_a n_b. \quad (4)$$

This implies that the original system with reabsorption can be equivalent to an effective system in which the reabsorption is absent, and the corresponding external quantities for this effective system are

$$\tilde{\gamma}_{e,r} = \eta_e \dot{\gamma}_{e,r}, \quad (5)$$

$$\tilde{\gamma}_{e,nr} = \dot{\gamma}_{e,nr}, \quad (6)$$

$$\tilde{\gamma}_{e,d} = \eta_e \dot{\gamma}_{e,r} + \dot{\gamma}_{e,nr}, \quad (7)$$

$$\tilde{\eta}_{e\text{-}ph} = \frac{\eta_e \dot{\gamma}_{e,r}}{\eta_e \dot{\gamma}_{e,r} + \dot{\gamma}_{e,nr}}. \quad (8)$$

These quantities are essentially affected by η_e, which can be calculated knowing the reabsorption coefficient and the medium geometry. The average reabsorption coefficient $\sigma_{ph,r}$ is determined by the overlap between the absorption and fluorescence spectra.[21] For a 2%-doped Yb^{3+}:ZBLAN, $\sigma_{ph,r}$ =0.266 cm^{-1},[21] and this value is used here for our estimation. For the thin cylinder medium, the average distance that a photon travels to escape the medium, L_{ave}, is estimated to be the diameter D. Then, the escape efficiency is approximated as

$$\eta_e = \exp(-\sigma_{ph,r} L_{ave}) = 0.995. \quad (9)$$

This is only 0.5% less than unity, due essentially to the small size of our sample. If the intrinsic quantum efficiency $\eta_{e\text{-}ph}$ is 0.99, then the external quantum efficiency is found using Eq. (8) to be

$$\tilde{\eta}_{e\text{-}ph} = 0.989\,95, \quad (10)$$

which differs from the intrinsic quantum efficiency $\eta_{e\text{-}ph}$ by only 0.005%. As a result, the red-shift of the mean fluorescence wavelength is also negligible. Therefore, for the small size medium considered here, the effect of reabsorption on the laser cooling performance is safely neglected in the analysis that follows, and η_e is assumed to be unity.

The absorption rate $\dot{\gamma}_{e,a}$ is proportional to the energy density of the pumping field, as[22]

$$\dot{\gamma}_{e,a} = B_{e,a} e_{ph,i}. \quad (11)$$

Here, the excitation coefficient $B_{e,a}$ has a similar role with the Einstein B coefficient.[22] Note that the Einstein B coefficient describes the photon-electron coupling strength on resonance, while here $B_{e,a}$ describes the phonon-assisted photon-electron coupling strength. In Eq. (11), $e_{ph,i}$ is the energy density of the pumping field inside the nanopowder, given by the following expression for a monochromatic electromagnetic wave:[23]

$$e_{ph,i} = \frac{1}{2} \epsilon_{e,r} |E|^2, \quad (12)$$

where $\epsilon_{e,r}$ is the real part of the permittivity of the medium, and $|E|$ is the amplitude of the local electric field. Alternatively, from the particle (photon) point of view, $e_{ph,i}$ can be written as

$$e_{ph,i} = \hbar \omega_{ph,i} n_{ph,i}, \quad (13)$$

where $n_{ph,i}$ is the number density of the pumping photons. Equations (12) and (13) are compatible in that they are the classical and quantum pictures of light.

At steady state, Eq. (2) becomes

$$\frac{dn_b}{dt} = -\dot{\gamma}_{e,d} n_b + \dot{\gamma}_{e,a} n_a = 0. \quad (14)$$

Since one excitation transition leads to the absorption of one incident photon with the energy $\hbar \omega_{ph,i}$ from the pumping field, the local absorbed power per unit volume is given by

$$\dot{s}_{ph,a} = \hbar\omega_{ph,i}\dot{\gamma}_{e,a}n_a = \hbar\omega_{ph,i}B_{e,a}n_ae_{ph,i}. \quad (15)$$

By definition, the absorption coefficient $\sigma_{ph,i}$ is given by

$$\sigma_{ph,i} = \frac{\dot{s}_{ph,a}}{I_{ph,i}} = \frac{\dot{s}_{ph,a}}{u_{ph,i}e_{ph,i}}, \quad (16)$$

where $I_{ph,i}$ and $u_{ph,i}$ are the intensity and speed of the pumping light. Substituting Eq. (15) into Eq. (16), we can write the absorption coefficient, a macroscopic quantity, in terms of atomistic scale quantities, as

$$\sigma_{ph,i} = \frac{\hbar\omega_{ph,i}B_{e,a}n_a}{u_{ph,i}}. \quad (17)$$

This indicates that the absorption coefficient $\sigma_{ph,i}$ is proportional to the excitation coefficient $B_{e,a}$, and the number density of absorbers n_a, as expected. The total absorbed power is then given by

$$Q_{ph,a} = \int_{V_s} \dot{s}_{ph,a}\, dV_s = \hbar\omega_{ph,i}\int_{V_s} \dot{\gamma}_{e,a}n_a\, dV_s. \quad (18)$$

The absorptance $\alpha_{ph,i}$ can then be calculated using

$$\alpha_{ph,i} = \frac{Q_{ph,a}}{Q_{ph,i}}. \quad (19)$$

Similarly, one radiative decay transition leads to the emission of a photon with a mean energy $\hbar\bar{\omega}_{ph,e}$. The total emitted power is thus given by

$$Q_{ph,f} = \hbar\bar{\omega}_{ph,e}\int_{V_s} \dot{\gamma}_{e,r}n_b\, dV_s. \quad (20)$$

Substituting Eqs. (3) and (14) into Eq. (20), we are able to write the emitted power in terms of the absorbed power as

$$Q_{ph,f} = \hbar\bar{\omega}_{ph,e}\eta_{e-ph}\int_{V_s} B_{e,a}n_ae_{ph,i}\, dV_s = \frac{\bar{\omega}_{ph,e}}{\omega_{ph,i}}\eta_{e-ph}Q_{ph,a}. \quad (21)$$

The net cooling power $\dot{S}_{ph-e-p}$ is then calculated as the difference between the absorbed and emitted radiation, i.e.,

$$\dot{S}_{ph-e-p} = Q_{ph,a} - Q_{ph,f} = \left(1 - \frac{\bar{\omega}_{ph,e}}{\omega_{ph,i}}\eta_{e-ph}\right)Q_{ph,a}$$

$$= \left(1 - \frac{\lambda_{ph,i}}{\bar{\lambda}_{ph,e}}\eta_{e-ph}\right)\hbar\omega_{ph,i}B_{e,a}n_a\int_{V_s} e_{ph,i}\, dV_s, \quad (22)$$

where we have assumed that in the solid phase the dopant concentration is spatially homogeneous (n_a is a constant). This definition indicates that a negative value of $\dot{S}_{ph-e-p}$ represents cooling. As a result, only those $\lambda_{ph,i}$ larger than $\bar{\lambda}_{ph,e}$ may result in cooling, and this range is defined as the cooling regime. Also, the quantum efficiency η_{e-ph} must be larger than $\bar{\lambda}_{ph,e}/\lambda_{ph,i}$, which is satisfied in cooling experiments on bulk crystals. Note that we have assumed that the quantum efficiency of nanopowders is the same as that of bulk materials. There are reports of decreased quantum efficiency in nanocrystals, due to surface defects, adsorbed gas molecules, or other quenching centers.[24]

The off-resonance absorption in laser cooling experiments is generally very small, and the system can thus be safely assumed to be far from saturation, i.e., the electronic population of the ground state is much larger than that of the excited state. As such, the ground state population can be approximated as the dopant concentration, i.e.,

$$n_a = n_d. \quad (23)$$

By defining a total pumping field energy inside the medium as

$$E_{pump} = \int_{V_s} e_{ph,i}\, dV_s, \quad (24)$$

the net cooling power becomes

$$\dot{S}_{ph-e-p} = \left(1 - \frac{\bar{\omega}_{ph,e}}{\omega_{ph,i}}\eta_{e-ph}\right)\hbar\omega_{ph,i}B_{e,a}n_dE_{pump}. \quad (25)$$

Thus, to enhance the cooling power using the same incident energy, increases in the dopant concentration n_d, the total pumping field energy inside the nanopowder medium E_{pump}, and the excitation coefficient $B_{e,a}$, are necessary. These effects will be discussed in the following sections for ion-doped nanopowders.

III. OPTIMUM DOPANT CONCENTRATION

A higher value of n_d, the dopant concentration, is desirable in laser cooling experiments, since more absorbers are available, which will compensate for the low absorption cross section. However, the negative side effect is that the excitation energy may hop around neighboring ions until it finds a quenching center to decay nonradiatively, as ions are closer to each other. This energy transfer mechanism leads to a drop in the quantum efficiency η_{e-ph}, and is an effect called the concentration quenching. Hence, an optimum dopant concentration, corresponding to a balance between the increase in n_d and the decrease in η_{e-ph}, should exist. However, due to the prior lack of a theory to describe this optimum concentration, arbitrary concentrations of 1 wt. % (corresponding to 2.42×10^{20} cm^{-3}) and 2 wt. % have been used in most of the existing experiments. In this section we suggest a criterion for determining the optimum concentration.

In highly pure Yb^{3+}-doped crystals, which are preferred in laser cooling experiments, nonradiative processes should be rather weak, and they essentially come from the self-generated quenching processes.[25,26] In such an event, one excited ion transfers its excitation energy to its identical neighbor, then to the lattice phonon modes, through a multiphonon relaxation process, as shown in Fig. 4. The neighbor ion ends up at its ground state. As the dopant concentration increases, the radiative decay rate remains unchanged, while the nonradiative decay rate increases due to the increase of the self quenching rate $\dot{\gamma}_{12}$, and as a result, the total decay rate is increased. This mechanism results in a decrease in both the lifetime of the excited state and the quantum efficiency.
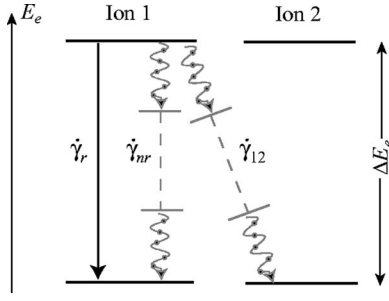
FIG. 4. Energy transfer scheme for the self-generated multiphonon assisted process $\dot{\gamma}_{12}$ between neighboring ions. The wavy lines indicate nonradiative transitions. $\dot{\gamma}_r$ and $\dot{\gamma}_{nr}$ are isolated ion radiative and nonradiative decay rates.

Based on the energy transfer theory, the excited state lifetime as a function of dopant concentration is[25]

$$\tau(n_d) = \frac{\tau(n_d = 0)}{1 + 1.45(n_d/n_{d,c})\exp[-\beta(E_p,T)\Delta E_e/4]}, \quad (26)$$

where $\tau(n_d=0)$ is the lifetime at an extremely low concentration, $n_{d,c}$ is defined as a critical concentration intrinsically dependent on the ion-host coupling, E_p is the phonon energy, ΔE_e is the energy gap between the two levels, and $\beta(E_p,T)$ is an energy transfer coefficient as a function of phonon energy and temperature. Here for Yb^{3+}: Y_2O_3, $\beta(E_p,T)$ is given by the following expression:[25]

$$\beta(E_p,T) = \frac{\ln[4.077/(1+f^o_{p,e})]}{\hbar\omega_{p,e}}, \quad (27)$$

where $\omega_{p,e}$ is the effective phonon frequency involved in the self-quenching process, and $f^o_{p,e}$ is the equilibrium distribution function of the phonon (the Bose-Einstein distribution), given by

$$f^o_{p,e} = \frac{1}{\exp(\hbar\omega_{p,e}/k_BT) - 1}. \quad (28)$$

Note that here we made an assumption of involving only one effective phonon mode $\omega_{p,e}$ in the self-quenching process. This approximation has proven very useful in understanding the multiphonon radiationless energy transfer processes of many rare-earth-doped solids, especially for systems involving weak coupling like Yb^{3+}:Y_2O_3 considered here. However, it must be noted that the frequency spectrum of phonons for any solid has a significant amount of structure in its DOS, and they may all contribute to the electron-phonon coupling. For physical systems involving strong coupling, the specific structure of the phonon spectra must be taken into account.[27]

Equation (26) predicts that the lifetime decreases as the dopant concentration increases. Since the lifetime is the reciprocal of the transition rate, one can rewrite Eq. (26) as

$$\dot{\gamma}_{e,d}(n_d) = \dot{\gamma}_{e,d}(n_d = 0)\{1 + 1.45(n_d/n_{d,c})\exp[\beta(E_p,T)\Delta E_e/4]\}, \quad (29)$$

where, based on the process shown in Fig. 4, we have

$$\dot{\gamma}_{e,d}(n_d = 0) = \dot{\gamma}_r + \dot{\gamma}_{nr}, \quad (30)$$

and

$$\dot{\gamma}_{e,d}(n_d) = \dot{\gamma}_r + \dot{\gamma}_{nr} + \dot{\gamma}_{12}. \quad (31)$$

It is predicted in Eq. (29) that an increase in n_d results in the increase in the total decay rate $\dot{\gamma}_{e,d}$, compared to that for an isolated ion, due to the presence of the self-generated, nonradiative decay rate $\dot{\gamma}_{12}$.

For an isolated Yb^{3+} ion in a Y_2O_3 host, the nonradiative decay rate $\dot{\gamma}_{nr}$ is negligible compared to the radiative decay rate $\dot{\gamma}_r$, below the room temperature (<300 K). Thus, we can make an approximation,

$$\frac{\dot{\gamma}_r}{\dot{\gamma}_r + \dot{\gamma}_{nr}} \simeq 1. \quad (32)$$

This indicates that the total decay rate at low concentration is taken as the radiative decay rate, and all nonradiative decay events come from the energy transfer processes.

Using Eqs. (29)–(32), the quantum efficiency η_{e-ph} can be written as a function of the concentration as

$$\eta_{e-ph} = \frac{\dot{\gamma}_r}{\dot{\gamma}_{e,d}(n_d)} = \frac{\gamma_r}{\dot{\gamma}_r + \dot{\gamma}_{nr}}\frac{\dot{\gamma}_r + \dot{\gamma}_{nr}}{\dot{\gamma}_{e,d}(n_d)}$$
$$= \{1 + 1.45(n_d/n_{d,c})\exp[-\beta(E_p,T)\Delta E_e/4]\}^{-1}. \quad (33)$$

It is predicted in this relation that the quantum efficiency decreases as the dopant concentration and temperature increase, as expected. The temperature effect is due to the fact that more phonons are excited and participate in the nonradiative processes. The total cooling power given by Eq. (22) is now written as a function of the concentration, i.e.,

$$\dot{S}_{ph-e-p} = \left(1 - \frac{\bar{\omega}_{ph,e}}{\omega_{ph,i}}\left[1 + 1.45\frac{n_d}{n_{d,c}}\exp(-\beta\,\Delta E_e/4)\right]^{-1}\right)$$
$$\times \hbar\omega_{ph,i}\dot{\gamma}_{e,a}n_d\int_V e_{ph,i}\,dV. \quad (34)$$

The maximum cooling power is reached when

$$\frac{\partial\dot{S}_{ph-e-p}}{\partial n_d} = 0, \quad (35)$$

which yields the optimum concentration

$$n^*_{d,o} = \frac{n_{d,o}}{n_{d,c}} = A\frac{(1-B)^{1/2}}{1-(1-B)^{1/2}}, \quad (36)$$

where A and B are

$$A = \frac{1}{1.45}\exp[\beta(E_p,T)\Delta E_e/4], \quad B = \frac{\lambda_{ph,e}}{\lambda_{ph,i}}. \quad (37)$$

It is evident in Eq. (36) that the critical concentration $n_{d,c}$ is the only parameter that needs to be specified before the optimum concentration can be determined. Note that $n_{d,c}$ is an intrinsic property depending on the ion-dopant pair and the temperature, and may be calculated using quantum me-
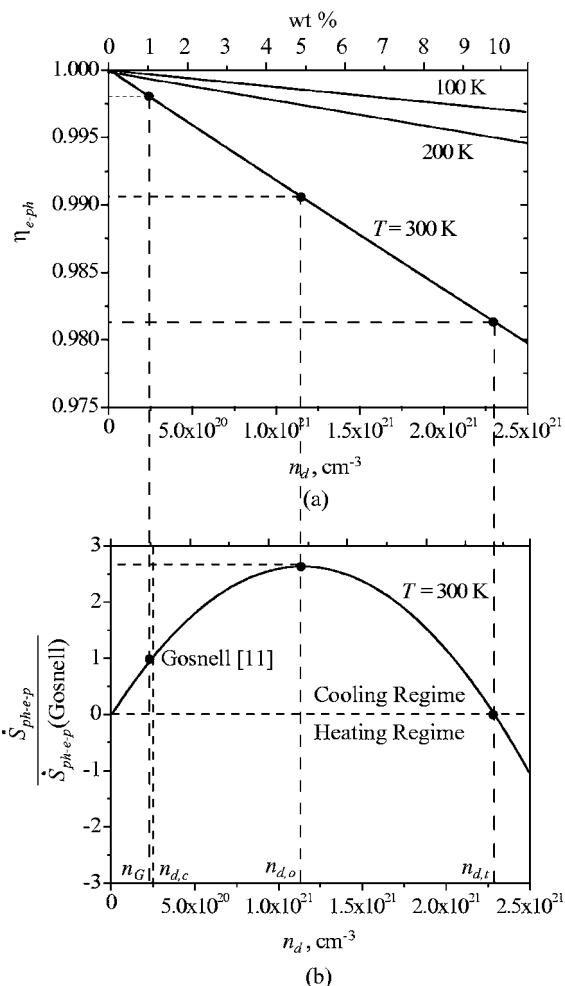
FIG. 5. (a) Variation of the quantum efficiency as a function of dopant concentration. (b) Variation of the normalized cooling power as a function of dopant concentration. The Gosnell $n_{d,G}$, critical $n_{d,c}$, optimum $n_{d,0}$, and transition $n_{d,t}$ dopant concentrations are shown.

chanics. Here, we use a more practical approach, namely, fitting Eq. (26) or Eq. (33) to experiments, as reported in Ref. 25.

In an experiment,[11] a Yb^{3+}-doped ZBLANP fiber was cooled by 65 K from room temperature, with a concentration $n_d=2.42\times10^{20}$ cm^{-3}, and a measured quantum efficiency $\eta_{e-ph}=0.998$. Using Eq. (33), the critical concentration is readily calculated to be $n_{d,c}=2.51\times10^{20}$ cm^{-3}. Then, by using Eq. (33), the variations of the quantum efficiency is plotted as a function of the concentration, for three temperatures, as shown in Fig. 5(a). The results show that the quantum efficiency η_{e-ph} decreases monotonically with the dopant concentration and temperature. By using Eq. (34), the variation of the normalized cooling power is plotted as a function of the concentration in Fig. 5(b). The results show that the cooling power first increases and then decreases, as n_d increases. At an optimum concentration, $n_{d,0}=1.13\times10^{21}$ cm^{-3}, which is three times higher than that used by Gosnell,[11] the maximum cooling power is achieved and is 2.6 times that obtained in that investigation.[11] Note that if the concentration becomes higher than a transition value $n_{d,t}$, which is 2.28×10^{21} cm^{-3}, the cooling effect is eliminated
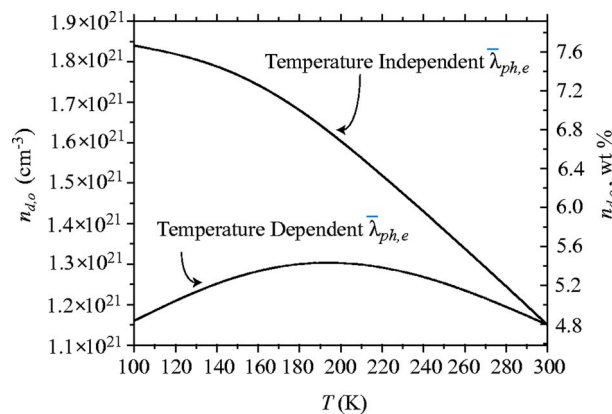

FIG. 6. (Color online) Variation of the optimum concentration as a function of temperature, for temperature independent and dependent $\bar{\lambda}_{ph,e}$.

[see Fig. 5(b)]. This is expected, due to the resulting low quantum efficiency.

To examine the dependence of the optimum concentration on temperature, we use Eq. (36), and the results are shown in Fig. 6. Since the quantum efficiency increases as the temperature decreases, we expect the optimum concentration to also increase. This is true, as shown in Fig. 6, if we assume that the mean emission wavelength $\bar{\lambda}_{ph,e}$ is not dependent on temperature. However, in reality, the mean emission wavelength $\bar{\lambda}_{ph,e}$ increases as the temperature decreases, since the electrons in the excited state are more likely to reside in the lowest sublevels, resulting in emission photons with a lower energy and a longer wavelength. Lei *et al.* performed an experimental study on the relation between $\bar{\lambda}_{ph,e}$ and T,[28] and their data are fitted by us using an empirical relation, which reads as $\bar{\lambda}_{ph,e}=1003+(996-1003)/(300-100)*(T-100)$ nm. Taking into account this dependence, the variation of the optimum concentration with temperature is shown in Fig. 6. Interestingly, it first increases, but then decreases, as the temperature decreases. The reason is that, at very low temperatures, the mean emission wavelength increases, leading to a reduction of the cooling ability per ion. As a result, the cooling effect is more likely to be destroyed by the nonradiative decays that can be caused by large concentrations. This variation of the optimum concentration with the temperature reflects the competition and balance between the quantum efficiency and the mean emission wavelength.

Before moving into photon absorption optimization, we note that even though this optimum concentration analysis is performed explicitly for nanocrystals, it is also applicable to bulk materials. A recent spectroscopic experiment[29] on a bulk material indicates that the optimum concentration may be around 4%–5%, validating our prediction.

IV. ENHANCED TOTAL PUMPING ENERGY BY PHOTON LOCALIZATION

In this section, we will discuss how to use the unique photon transport properties of nanopowders to enhance
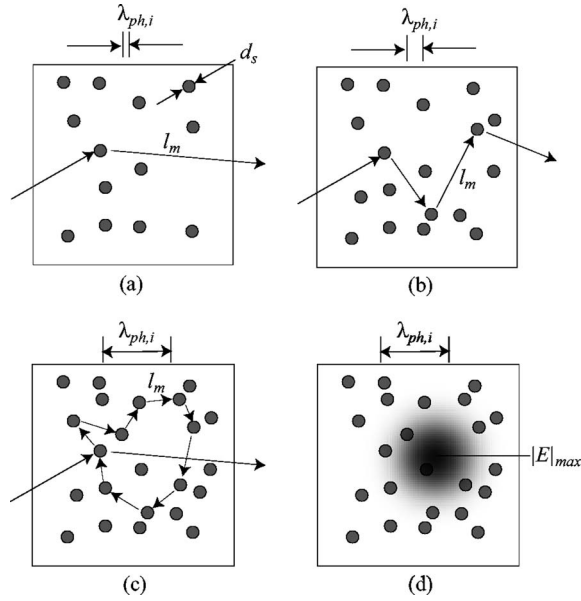
FIG. 7. (a) Single, (b) multiple, and (c) recurrent photon scattering trajectories in a system of random scatterers, and (d) a rendering of the electromagnetic field distribution for case (c), i.e., as photon localization takes place (Ref. 30).
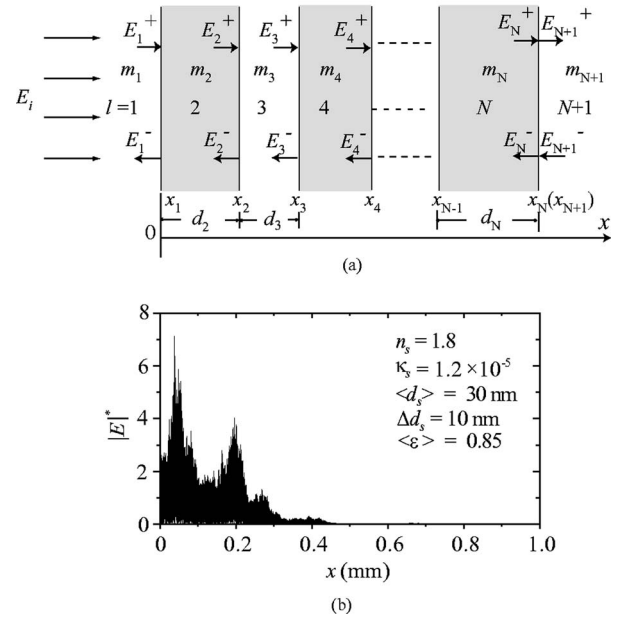

FIG. 8. (a) A one-dimensional random multilayer system. The layer thickness follows a uniform distribution between $\langle d_s \rangle \pm \Delta d_s$, and the porosity is prescribed. (b) A typical electromagnetic field distribution, in which a field enhancement up to seven folds can be seen (Ref. 37).

E_{pump}, the total pumping energy inside the medium. Shown in Fig. 7 are different regimes of photon scattering in nanopowders.[30] When the photon mean free path l_m is much larger than the laser wavelength, photons may experience a single scattering event, and the transport is diffusive.[31] As l_m decreases, photons begin to undergo multiple scattering events. When l_m is comparable to or smaller than the laser wavelength, recurrent scattering takes place, i.e., photons return to the original place after being scattered many times. In this case, photons do not propagate through the medium, but are confined in a small spatial region, forming a cavity. This phenomenon, termed photon localization, is the counterpart of the electron localization suggested by Anderson.[32] The electromagnetic field of the localized light, as shown in Fig. 7(d), can be orders of magnitude higher than the incident field.[33] Note that the onset of photon localization is generally questionable when the medium becomes dissipative, since one cannot distinguish whether the attenuation of intensity is caused by strong scattering or by strong absorption. However, for doped nanopowders considered in this analysis, the medium is only slightly dissipative (a very low absorption coefficient). As such, the medium is mainly a strongly scattering medium rather than an absorbing medium, and the attenuation of intensity is dominated by photon localization.[33] This has been confirmed in many random laser experiments on ion-doped powder media.[34,35] As a result of the photon localization, the photon absorption can be enhanced considerably, due to this high photon density (or alternatively, electromagnetic field energy density $e_{ph,i}$).

Here, we consider a simple nanostructure model of Yb^{3+}-doped Y_2O_3 particles: parallel solid layers with random thicknesses, as shown in Fig. 8(a). The dielectric solid material has a complex refractive index m_s ($=n_s+i\kappa_s$), while the fluid is assumed to be air and has a refractive index

m_f ($=n_f=1$). To solve the internal field subject to a normal laser irradiation, we start with the Helmholtz equation,

$$\frac{d^2E(x)}{dx^2} + k_0^2 m_l^2 E(x) = 0, \qquad (38)$$

where k_0 is the vacuum wave vector, and m_l is the local complex index of refraction at the incident frequency. This is the electromagnetic wave equation in a source-free medium, and is equivalent to the Maxwell equations in the multilayer system. For the medium shown in Fig. 8(a), the solution of Eq. (38) at a particular location x_l in the lth layer is given by

$$E(x) = E_l^+ e^{ik_l(x-x_l)} + E_l^- e^{-ik_l(x-x_l)}, \quad l=1,2,\ldots,N+1,$$
$$(39)$$

where $k_l = m_l \omega_0 / c_0$ is the wave vector, and c_0 is the speed of light in vacuum. The field in the medium is divided into two components: the forward (transmitted) component E_l^+ and the backward (reflected) component E_l^-. The boundary conditions require that the tangential electric and magnetic fields be continuous across each interface. Thus, the amplitudes of the lth and $(l+1)$th interfaces are related by a transfer matrix M.[33,36] Then, the full fields E are solved using this transfer matrix approach, subject to a uniform, normal incident field E_i. A detailed solution procedure can be found in Refs. 33 and 37. A typical field distribution is shown in Fig. 8(b), where the dimensionless electric field $|E|^*$ is normalized against the incident field. The phenomenon of field enhancement is evident, i.e., the peaks of the field distribution inside the medium can be much larger than the incident field, for this realization.[33] Thus, the energy density of the electric field can be two or even more orders of magnitude larger
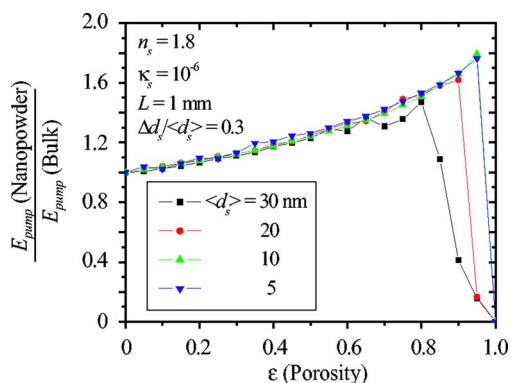
FIG. 9. (Color online) Variation of the scaled pumping energy inside the medium (nanopowder to the bulk crystal), with respect to porosity. The total pumping energy of nanopowder can be enhanced by 50%–70%, at high porosities.

than the incident value. The physical basis of field enhancement is electromagnetic wave interference. In this random multilayer system, the waves will multiply, transmit, and reflect at all the interfaces, and interfere with each other. At some locations (for some realizations), the interference is so ideally constructive that it results in extremely large fields.

The pumping energy E_{pump} inside the nanopowder medium is then calculated using Eq. (9), and compared to that for the bulk crystal with the same apparent volume (note, however, that the volume of the solid phase for nanopowder is smaller than that for the bulk crystal), as shown in Fig. 9. Note also that for a model composite given the porosity ϵ and the particle size distribution, there are an infinite number of realizations, and, hence, the ensemble average of a sufficient number of realizations is taken in calculations, and used for that model composite. The ratio of the total pumping energy, with respect to porosity ϵ for different particle mean diameter $\langle d_s \rangle$, is shown in Fig. 9. For high porosities, the ratio may be as large as 1.5 to 1.7, indicating an enhancement of the total pumping energy E_{pump} by 50% to 70%. Figure 9 also provides the guidelines for the optimum porosity and mean particle size.

It should be noted that the multiple scattering can also enhance the fluorescence reabsorption, which is a negative side effect. The 50% enhancement in the total pumping energy implies that the incident photons travel a 50% longer pathlength due to the multiple scattering, and it is reasonable to assume that L_{ave}, the average distance that a photon travels to escape from the medium, is also enhanced by 50% compared to that of the bulk. Then the escape efficiency η_e becomes

$$\eta_e = \exp(-\sigma_{ph,r} L_{ave}) = 0.993. \qquad (40)$$

This is very close to 0.995 for the bulk medium. Also, if the intrinsic quantum efficiency $\eta_{e\text{-}ph}$ is 0.99, then the external quantum efficiency becomes

$$\widetilde{\eta}_{e\text{-}ph} = 0.989\,93. \qquad (41)$$

This is almost the same as that (0.989 95) for the bulk medium. Therefore, the reabsorption effect of photon localiza-

tion in nanopowder medium can be neglected.

In this section we have used light multiple scattering to enhance the total pumping energy in nanopowder media. Similar enhancements can also be applied to bulk materials. For example, the sample can be placed in a multipass external cavity, in which mirrors are used to reflect the unabsorbed pumping light back to the sample, leading to the upper limit of absorption of the pumping power.[17] The bulk sample can also be placed in an intracavity laser, in which the optical energy density is intrinsically multiple pass. Discussions on this scheme and a comparison with the extracavity scheme have been given in Refs. 16 and 38.

V. ENHANCED TRANSITION PROBABILITY FOR NANOPOWDERS

A. Phonon DOS of the nanopowder

To analyze photon-electron-phonon interactions, the phonon DOS needs to be known. The Debye DOS is often assumed for bulk materials.[39] It shows a parabolic distribution that results from an assumption of an isotropic medium with no dispersion, or effects of optical phonons. The phonon DOS of nanostructures may, however, deviate from that for bulk crystals, due to quantum size effects.[40] Since the phonon DOS is not available for Y_2O_3, it is calculated here using the molecular dynamics simulation.

With molecular dynamics simulations, the phonon DOS may be calculated using three different methods.[41] In the first, the velocity autocorrelation function is calculated for each species and the partial phonon DOS is then obtained by taking the Fourier transforms of this autocorrelation function. In the second, the displacement autocorrelation function is calculated by the equation-of-motion method. In the third, the dynamical matrix is directly diagonalized. The results of these three approaches have been found to agree with one another at low temperatures,[41] as expected. However, at high temperature the third method is not suitable, since it is harmonic. Therefore, here we use the first method to determine the phonon DOS at 300 K.

In a molecular dynamics simulation, the phase-space trajectory of a system of particles is predicted by solving the Newton equations. The required inputs are an atomic structure and a suitable interatomic potential, which can be obtained from experiments and/or *ab initio* calculations.[42]

The x-ray diffraction[43] and neutron diffraction[44] experiments have shown that Y_2O_3 has a face-centered cubic structure, which is retained in nanocrystals.[45] Eight metal ions are in the positions $(1/4, 1/4, 1/4)$; the remaining 24 occupy the sites $(u, 0, 1/4)$. The 48 oxygen ions are in general positions (x, y, z), arranged in distorted octahedra around the metal ions, the metal-oxygen bonding distances being unequal. The values of u, x, y, z are listed in Refs. 43 and 44. The crystal structure is shown in Fig. 10.

The interatomic potential can be assumed to be in the form

$$\varphi(r_{ij}) = \frac{q_i q_j}{r_{ij}} + A_{ij} \exp\left(-\frac{r_{ij}}{r_{0,ij}}\right) + \frac{C_{ij}}{r_{ij}^6}, \qquad (42)$$

where $\varphi(r_{ij})$ is the interaction energy of atoms i and j, which consists of a Coulomb term and a covalent (short range)
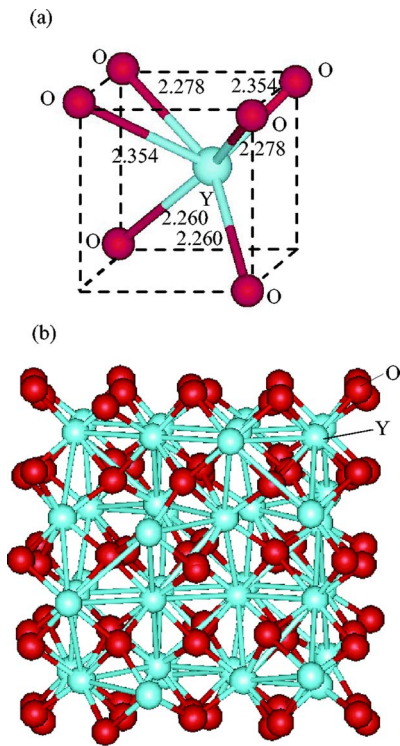
(a)

(b)

FIG. 10. (Color online) Crystal structure of Y_2O_3. (a) The oxygen ions are arranged in distorted octahedra around the Yttrium ions. The listed measured equilibrium bond lengths are in Å. (b) The structure of a cubic unit cell.

contribution, cast into the usual Buckingham form.[46] Here q_i is an effective charge of the ith atom, r_{ij} is the interatomic distance between atoms i and j, and A_{ij}, $r_{0,ij}$, and C_{ij} are parameters for covalent interactions. For ionic materials, this Buckingham interatomic potential model has been shown to perform well. The parameters in Eq. (42), obtained from Refs. 47 and 48, are listed in Table I. This potential set has been verified to reproduce the bulk properties (lattice constant, lattice position, bulk modulus, elastic constant, etc) well.[49]

To determine the DOS of the bulk crystal, molecular dynamics simulations are carried out in a cubic computation domain that contains $2 \times 2 \times 2 = 8$ unit cells and $N = 640$ atoms (256 Y and 384 O). The MD code, which was developed by Dr. McGaughey and was used to model the thermal conductivity,[50] has been used. Periodic boundary conditions are applied in all directions. For the nanopowder, the computation domain is a sphere of diameter d_s, which is cut from a much larger bulk crystal, as shown in Fig. 11. It should be noted that a nanopowder generated in this way may not be

TABLE I. Parameters used in the Buckingham potential. Atomic charges: $q_Y = 3$, $q_O = -2$.

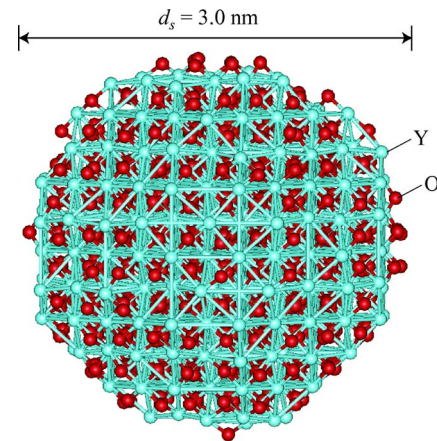| Atom-atom	A_{ij}, eV	$r_{0,ij}$, Å	C_{ij}, eV Å	References
Y-Y	0	1	0	48
Y-O	1345.6	0.3491	0	47 and 48
O-O	22799	0.149	27.93	47 and 48

$d_s = 3.0$ nm

FIG. 11. (Color online) The structure of the spherical Y_2O_3 nanoparticle (cluster) used in the molecular dynamics simulations. The diameter is 3 nm (about 1000 atoms) and the boundary is free.

neutral in charge, thus some atoms at the surface may need to be removed accordingly, to eliminate any net charge of the nanopowder. Also, since the center of the sphere can be randomly selected, we have many possible configurations given the diameter. As such, a number of spherical particles with different configurations are considered in this study, and their behaviors are compared. The free boundary condition is used.

For both bulk and nanocrystals, an initialization period of 5×10^4 time steps is used, with the time step being 1.6 fs. The system is run in the NVT (constant mass, volume, and temperature) ensemble. To set the temperature for the NVT ensemble, the potential energy of the system is monitored every time step. When it reaches a value within 10^{-4}% of the desired value, the ensemble is switched to NVE (constant mass, volume, and energy), and the system is run until the total number of time steps is 1.5×10^5.

The normalized velocity-velocity autocorrelation function for the βth species ($\beta = Y, O$) is

$$\Gamma_\beta(t) = \left\langle \sum_{i_\beta=1}^{N_\beta} \mathbf{u}_{i_\beta}(t)\mathbf{u}_{i_\beta}(0) \right\rangle \Bigg/ \left\langle \sum_{i_\beta=1}^{N_\beta} \mathbf{u}_{i_\beta}(0)\mathbf{u}_{i_\beta}(0) \right\rangle,$$

$$\beta = Y, O, \tag{43}$$

where N_β is the number of atoms of species β, $\mathbf{u}_{i_\beta}$ is the velocity of atom i_β and $\langle \rangle$ is an ensemble average. The frequency spectrum of the normalized velocity autocorrelation function gives the partial phonon DOS $D_{p,\beta}(\omega)$, as

$$D_{p,\beta}(\omega) = \int_0^\tau \Gamma_\beta(t)\cos(\omega t)dt. \tag{44}$$

The total phonon DOS is obtained by summing over the partial DOS weighted with the population, i.e.,
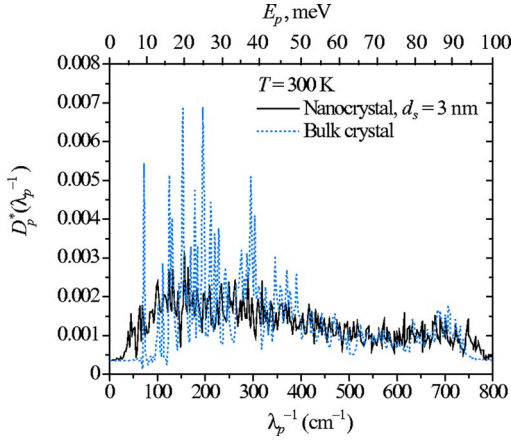
FIG. 12. (Color online) A comparison of the phonon DOS of the bulk crystal and nanocrystal for Y_2O_3. The nanocrystal DOS possesses extended low- and high-frequency tails.

$$D_p(\omega) = \sum_\beta c_\beta D_{p,\beta}(\omega), \tag{45}$$

where c_β is the population of the βth species in the molecular dynamics system. Here, for Y_2O_3 they are $c_Y = 2/5$ and $c_O = 3/5$.

The partial phonon DOS $D_{p,\beta}(\omega)$ of Y and O atoms are calculated for the bulk and nanoparticle Y_2O_3 crystals, and are normalized, i.e., $\int_0^\infty D_{p,\beta}(\omega)d\omega = 1$. This normalization is needed to compare the partial and total DOS of MD systems with different number of atoms. The total DOS, calculated using Eq. (45), is then shown in Fig. 12. As mentioned before, there are many different configurations for the nanopowder, each having its own phonon DOS. However, calculations review that they share similar characteristics. Therefore, here we only show the DOS of one representative configuration. It can be seen that the phonon DOS of nanocrystals is distinct from that of the bulk crystal, in its broadened peaks, and extended tails at low and high frequencies. The bulk crystal has sharp, well-defined peaks (or modes) related to the rigorous periodic structure, while these peaks are broadened in the nanocrystal, due to the loss to some extent of this periodicity. The high frequency tail in the nanocrystal phonon DOS is believed to result from the surface atoms. Due to the loss of the attraction from their outer neighbors, these atoms have contracted bonds with their inner neighbors, compared to the bulk crystal. This leads to a "harder" surface and increased vibrational frequencies.

Here we have suggested modification of the phonon DOS due to the finite-small size of the nanocrystals. For the bulk materials, the phonon DOS can also be engineered using different host materials. We note that this would also alter the ion-phonon coupling.

B. Excitation rate: A Fermi golden rule calculation

As the pumping wavelength is tuned to the red side of the resonance, the probability of a purely electronic transition between electronic sublevels, a first-order process, becomes smaller. On the other hand, the phonon-assisted transition, a

second-order process, starts to contribute significantly to absorption. As a result, the absorption turns out to be a combination of the first- and second-order transitions. Since a much longer pumping wavelength than the resonance is used in laser cooling, the total transition is believed to be dominated by the second-order process. Therefore, only the second-order process will be analyzed here for the purpose of understanding the role of phonons in laser cooling.

In the second-order process, the ion in its ground state absorbs a photon from the irradiation and, simultaneously, a phonon from the lattice, and goes up to the excited state. The probability per unit time of such a process can be evaluated using the perturbation theory. The Hamiltonian for the physical system considered is given by[12]

$$H = H_{ion} + H_p + H_{ph} + \varphi_{ion\text{-}ph} + \varphi_{ion\text{-}p}. \tag{46}$$

The first term is

$$H_{ion} = \hbar\omega_{e,g}a^+a, \tag{47}$$

i.e., the Hamiltonian of the ion electronic levels, where $\hbar\omega_{e,g}$ is the energy difference between the optically active energy levels of the dopant ion (considered as a two-level ion) and $a^+(a)$ is the creation (annihilation) operator of an electronic excitation. The second term is

$$H_p = \sum_p \hbar\omega_p b_p^+ b_p, \tag{48}$$

i.e., the phonon field Hamiltonian, where ω_p is the phonon frequency and $b_p^+(b_p)$ is the creation (annihilation) operator of a phonon in mode p. The third term is

$$H_{ph} = \hbar\omega_{ph,i}c^+c, \tag{49}$$

i.e., the electromagnetic laser field Hamiltonian, where $\omega_{ph,i}$ is the pumping frequency and $c^+(c)$ is the creation (annihilation) operator of a photon. The fourth term is

$$\varphi_{ion\text{-}ph} = -\mathbf{e}_\alpha \cdot \boldsymbol{\mu}_e \left(\frac{\hbar\omega_{ph,i}}{2\epsilon_0 V_s}\right)^{1/2}(a^+ + a)(c^+ + c)$$

$$= C_{ph}(a^+ + a)(c^+ + c),$$

$$C_{ph} = -\mathbf{e}_\alpha \cdot \boldsymbol{\mu}_e \left(\frac{\hbar\omega_{ph,i}}{2\epsilon_0 V_s}\right)^{1/2}, \tag{50}$$

i.e., the ion-photon interaction Hamiltonian, where, as mentioned before, $\mathbf{e}_\alpha$ is the polarization factor of the photon, $\boldsymbol{\mu}_e$ is the dipole moment of the electronic transition, ϵ_0 is the vacuum permittivity, and V_s is the interacting volume. Note that the term $[\hbar\omega_{ph,i}/(2\epsilon_0 V_s)]^{1/2}$ is the electric field per photon. The fifth term is

$$\varphi_{ion\text{-}p} = a_{i\text{-}p} \left(\frac{\hbar\omega_p}{2\rho u_p^2}\right)^{1/2} a^+ a(b_p - b_p^+) = C_p a^+ a(b_p - b_p^+),$$

$$C_p = a_{i\text{-}p} \left(\frac{\hbar\omega_p}{2\rho u_p^2}\right)^{1/2}, \tag{51}$$

i.e., the ion-phonon interaction Hamiltonian, where $a_{i\text{-}p}$ is the ion-phonon coupling constant and is purely imaginary, u_p is the speed of sound, and ρ is the mass density.

The transition rate $\dot{\gamma}_{e,a}$ is given by the Fermi golden rule[12]

$$\dot{\gamma}_{e,a} = \sum_f \dot{\gamma}_{e,i\text{-}f} = \frac{2\pi}{\hbar} \sum_f |M_{fi}|^2 \delta(E_f - E_i), \qquad (52)$$

where E_i and E_f are the initial and final energies of the system. The M_{fi} matrix can be expanded as the following series:[12]

$$M_{fi} = \langle f|\varphi_{int}|i\rangle + \sum_m \frac{\langle f|\varphi_{int}|m\rangle\langle m|\varphi_{int}|i\rangle}{E_{e,i}^T - E_{e,m}^T}$$

$$+ \sum_{m,n} \frac{\langle f|\varphi_{int}|m\rangle\langle m|\varphi_{int}|n\rangle\langle n|\varphi_{int}|i\rangle}{(E_{e,i}^T - E_{e,m}^T)(E_{e,i}^T - E_{e,n}^T)} + \dots, \quad (53)$$

with $\varphi_{int} = \varphi_{ion\text{-}ph} + \varphi_{ion\text{-}p}$. The summations on m and n include all the intermediate phonon and photon states.

We will calculate the transition probability rate $\dot{\gamma}_e$ between the initial $|i\rangle = |\psi_i, f_{ph}+1, f_p+1\rangle$ and final $|f\rangle = |\psi_f, f_{ph}, f_p\rangle$ states of the system, where the first ket element, ψ_i, refers to the ion state, the second one, f_{ph}, to the photon number in the interacting volume V_s, and the third one, f_p, to the phonon distribution function. This type of process only appears in the second-order perturbation expansion of the M_{fi} matrix, which is[27,51]

$$M_{fi,2nd} = \sum_m \frac{\langle f|\varphi_{int}|m\rangle\langle m|\varphi_{int}|i\rangle}{E_{e,i}^T - E_{e,m}^T} = \sum_m \left[\frac{\langle \psi_f, f_{ph}, f_p|\varphi_{ion\text{-}ph}|\psi_m, f_{ph}+1, f_p\rangle \times \langle \psi_m, f_{ph}+1, f_p|\varphi_{ion\text{-}p}|\psi_i, f_{ph}+1, f_p+1\rangle}{E_i - (E_m - \hbar\omega_p)} \right.$$

$$\left. + \frac{\langle \psi_f, f_{ph}, f_p|\varphi_{ion\text{-}p}|\psi_m, f_{ph}, f_p+1\rangle \times \langle \psi_m, f_{ph}, f_p+1|\varphi_{ion\text{-}ph}|\psi_i, f_{ph}+1, f_p+1\rangle}{E_i - (E_m - \hbar\omega_{ph})} \right]. \qquad (54)$$

The sum runs over all possible intermediate states of the system. Substituting the expressions for the interaction Hamiltonians into Eq. (54), we have

$$M_{fi,2nd} \simeq \sum_m \frac{\langle \psi_f, f_{ph}, f_p|C_{ph}(a^+ + a)(c^+ + c)|\psi_m, f_{ph}+1, f_p\rangle \times \langle \psi_m, f_{ph}+1, f_p|a_{i\text{-}p}C_p a^+ a(b_p - b_p^+)|\psi_i, f_{ph}+1, f_p+1\rangle}{E_i - (E_m - \hbar\omega_p)}$$

$$= \sum_m \frac{\langle \psi_f, f_{ph}, f_p|C_{ph}(a^+ + a)(c^+ + c)|\psi_m, f_{ph}+1, f_p\rangle \times \langle \psi_m, f_{ph}+1, f_p|C_p a^+ a(b_p - b_p^+)|\psi_i, f_{ph}+1, f_p+1\rangle}{E_i - (E_m - \hbar\omega_p)}$$

$$= \sum_m \frac{\langle \psi_f, f_{ph}, f_p|C_{ph}(a^+ + a)f_{ph}^{1/2}|\psi_m, f_{ph}, f_p\rangle \times \langle \psi_m, f_{ph}+1, f_p|C_p a^+ a f_p^{1/2}|\psi_i, f_{ph}+1, f_p\rangle}{E_i - (E_m - \hbar\omega_p)}$$

$$= \sum_m C_{ph} f_{ph}^{1/2} C_p f_p^{1/2} \frac{\langle \psi_f|(a^+ + a)|\psi_m\rangle\langle \psi_m|a^+ a|\psi_i\rangle}{E_i - (E_m - \hbar\omega_p)}, \qquad (55)$$

where the second term in Eq. (54) has been neglected since the photon energy is much greater than the phonon energy.[27]

Since the phonon energy $\hbar\omega_p$ is much smaller than the energy gap, it cannot by itself induce an electronic transition. In the perturbation theory, the intermediate wave function ψ_m is then approximated as unperturbed, i.e., $\psi_m = \psi_i$, and $E_m = E_i$. Therefore Eq. (55) becomes

$$M_{fi,2nd} = \sum_p C_{ph} f_{ph}^{1/2} C_p f_p^{1/2} \frac{\langle \psi_f|(a^+ + a)|\psi_i\rangle\langle \psi_i|a^+ a|\psi_i\rangle}{E_i - (E_i - \hbar\omega_p)} = \sum_p C_{ph} f_{ph}^{1/2} C_p f_p^{1/2} \frac{\langle \psi_f|(a^+ + a)|\psi_i\rangle\langle \psi_i|a^+ a|\psi_i\rangle}{E_i - (E_i - \hbar\omega_p)} = \sum_p C_{ph} f_{ph}^{1/2} C_p f_p^{1/2} \frac{1}{\hbar\omega_p}. \qquad (56)$$

Substituting Eq. (56) into Eq. (52), we have

$$\dot{\gamma}_{e,a} = \sum_f \dot{\gamma}_{e,i\text{-}f} = \frac{2\pi}{\hbar} \sum_p \left(\frac{C_{ph}|C_p|}{\hbar\omega_p} \right)^2 f_{ph} f_p \delta(\hbar\omega_{ph,i} + \hbar\omega_p - \hbar\omega_{e,g}). \qquad (57)$$

In order to perform the summation on the phonon modes in Eq. (57), we must introduce the phonon DOS $D_p(E_p)$, where E_p is the phonon energy given by $E_p = \hbar\omega_{e,g} - \hbar\omega_{ph,i}$. In terms of this distribution function, the transition rate, Eq. (57), becomes

$$\dot{\gamma}_{e,a} = \frac{2\pi}{\hbar} C_{ph}^2 f_{ph} \frac{|a_{i\text{-}p}|^2}{2\rho u_p^2} \int_{E_{min}}^{E_{max}} dE_p \, D_p(E_p) \frac{f_p^0(E_p)}{E_p}$$

$$\times \delta(\hbar\omega_{ph,i} + E_p - \hbar\omega_{e,g})$$

$$= \frac{2\pi}{\hbar} C_{ph}^2 f_{ph} \frac{|a_{i\text{-}p}|^2}{2\rho u_p^2} \frac{D_p(E_p) f_p^0(E_p)}{E_p}. \quad (58)$$

This result implies that the excitation spectra can be associated with the phonon spectra, as observed in Ref. 52. Here we have used the equilibrium distribution functions for phonons. To compare with Eq. (11), we rewrite Eq. (58) as

$$\dot{\gamma}_{e,a} = \frac{2\pi}{\hbar} \frac{(\mathbf{e}_\alpha \cdot \boldsymbol{\mu}_e)^2}{2\epsilon_0} \frac{|a_{i\text{-}p}|^2}{2\rho u_p^2} \frac{D_p(E_p) f_p^0(E_p)}{E_p} \hbar\omega_{ph,i} \frac{f_{ph}}{V_s}$$

$$= \frac{2\pi}{\hbar} \frac{(\mathbf{e}_\alpha \cdot \boldsymbol{\mu}_e)^2}{2\epsilon_0} \frac{|a_{i\text{-}p}|^2}{2\rho u_p^2} \frac{D_p(E_p) f_p^0(E_p)}{E_p} e_{ph,i}. \quad (59)$$

This expression is found to be consistent with Eq. (11), as expected. Therefore, we are able to extract the excitation coefficient $B_{e,a}$ from Eq. (59), as

$$B_{e,a} = \frac{2\pi}{\hbar} \frac{(\mathbf{e}_\alpha \cdot \boldsymbol{\mu}_e)^2}{2\epsilon_0} \frac{|a_{i\text{-}p}|^2}{2\rho u_p^2} \frac{D_p(E_p) f_p^0(E_p)}{E_p}. \quad (60)$$

Using the relations $\omega = 2\pi c_0/\lambda$ and $E_p = \hbar\omega_{e,g} - \hbar\omega_{ph,i}$, the above expression for $B_{e,a}$ can be written as a function of $\lambda_{ph,i}$ as

$$B_{e,a} = \frac{2\pi}{\hbar} \frac{(\mathbf{e}_\alpha \cdot \boldsymbol{\mu}_e)^2}{2\epsilon_0} \frac{|a_{i\text{-}p}|^2}{2\rho u_p^2}$$

$$\times \frac{D_p\left(\hbar\frac{2\pi c_0}{\lambda_{e,g}} - \hbar\frac{2\pi c_0}{\lambda_{ph,i}}\right) f_p^0\left(\hbar\frac{2\pi c_0}{\lambda_{e,g}} - \hbar\frac{2\pi c_0}{\lambda_{ph,i}}\right)}{\hbar\frac{2\pi c_0}{\lambda_{e,g}} - \hbar\frac{2\pi c_0}{\lambda_{ph,i}}}.$$

$$(61)$$

Using the resonance wavelength ($\lambda_{e,g} = 980$ nm) for Yb^{3+}:Y$_2$O$_3$ along with the phonon DOS determined in Sec. V A, the variations of the normalized (against the resonance) transition coefficient $B_{e,a}^* = B_{e,a}(\lambda_{ph,i})/B_{e,a}(\lambda_{ph,i} = 980$ nm$)$, as a function of the pumping wavelength $\lambda_{ph,i}$, are shown in Fig. 13(a), for bulk and nanocrystals. Note that a singularity exists for $B_{e,a}(\lambda_{ph,i})$ right on resonance $\lambda_{ph,i} = 980$ nm, so we use the limit $B_{e,a}(\lambda_{ph,i} = 980$ nm$) = B_{e,a}(\lambda_{ph,i} \rightarrow 980$ nm$)$. The transition coefficients show an exponential decay with the increasing wavelength. Shown in Fig. 13(b) is the ratio of the transition rates for nano- and bulk crystals. The transition rates may be enhanced (the area above the dotted line) or reduced (the area below the dotted line), depending on the pumping wavelength used. However, in the practical cooling range ($\lambda_{ph,i} = 1020$ to 1030 nm) used in most experiments, more enhancement is observed than reduction.

VI. DISCUSSION AND CONCLUSIONS

We have investigated the enhanced laser cooling of nanopowders, using the optimization of the dopant concentra-
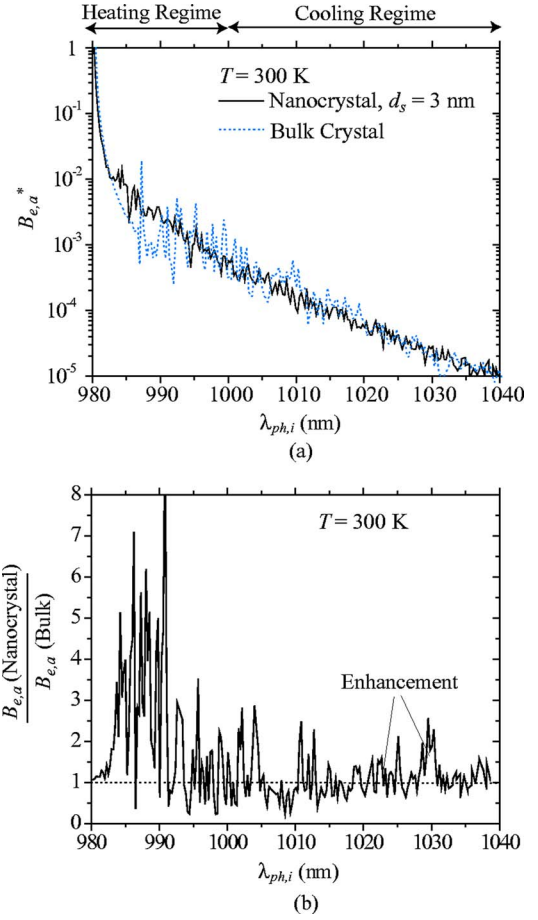

FIG. 13. (Color online) (a) Variations of the normalized (against the resonance) electronic transition coefficient $B_{e,a}^* = B_{e,a}(\lambda_{ph,i})/B_{e,a}(\lambda_{ph,i} = 980$ nm$)$ with respect to the laser pumping wavelength, for the bulk and the nanoparticle crystals, for Yb^{3+}:Y$_2$O$_3$. (b) The ratio of the transition coefficients for the nanocrystal and the bulk crystal.

tion, the photon localization, and the phonon DOS size effect. Taking a closer look at these three mechanisms, we notice that they all facilitate to increase the carrier number in the interacting volume: optimization of the dopant concentration for higher electron number, photon localization for higher photon number, and phonon DOS size effect for higher phonon number in the desired range. This seems to be straightforward since the excitation is a photon induced, phonon assisted, electronic absorption. Thinking of an interaction of only one photon, one phonon, and one electron (ion) as the base system, to increase the number of each type of carrier would independently enhance the excitation events proportionally. This is an important yet intuitive finding that more carriers are needed to be put in the same interacting volume, to enhance their interactions. The enhancement effects due to each carrier are summarized in Fig. 14.

The optimum dopant concentration is pursued using the energy transfer theory. Although it is well known that an optimum concentration for maximum cooling performance should exist (since a high concentration would result in a low quantum efficiency), a quantitative analysis had been lacking. Here, we apply the energy transfer theory and obtain an
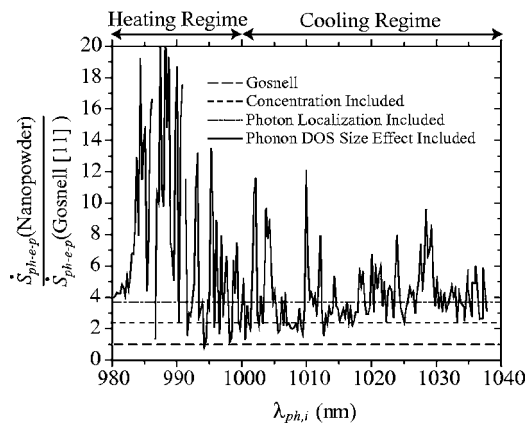
FIG. 14. Enhancement of laser cooling power by (i) optimization of the dopant concentration, (ii) photon localization, and (iii) the phonon DOS size effect. The baseline is the experiment of Gosnell (Ref. 11). The cooling and heating regimes are shown.

analytical expression for the optimum concentration. For high purity doped solids, the concentration quenching is identified as a self-generated multiphonon decay process, allowing us to establish a relation between the quantum efficiency and the concentration. The results show that the optimum concentration gives a 150% enhancement in cooling power, as shown in Fig. 14. This enhancement mechanism applies to both the bulk and the nanoparticle crystals doped with Yb^{3+}.

The cooling performance in nanocrystals may also be enhanced compared to that of bulk crystals, due to photon localization. Calculations based on the Maxwell equations show that as the particle size decreases to the order of the pumping wavelength, photons are localized in the interior of the powder media due to recurrent scattering. As a result, the total pumping energy (or the photon density) is enhanced, leading to an enhanced absorptivity. This mechanism is expected to have a 50% enhancement on the cooling power for nanopowders, compared to the bulk crystals, as shown in Fig. 14. It is shown that the reabsorption is negligible.

The phonon DOS size effect is also considered. The phonon DOS of a nanoparticle crystal is determined using molecular dynamics simulations and the Fourier transform of the velocity autocorrelation function. The DOS of nanocrystals possesses the extended, small tails at low and high frequencies. Treating the cooling process as a phonon-assisted transition, a second-order quantum mechanical calculation is performed to predict the transition rates. As shown in Fig. 14, this mechanism may enhance or reduce the cooling performance, depending on the pumping wavelength used. In the practical cooling range ($\lambda_{ph,i}$=1020 to 1030 nm), more enhancement is shown than reduction. If the broadening of the absorption spectra is taken into account, we can conclude that the phonon size effect would generally enhance the cooling performance.

Considering all these three mechanisms, the cooling power is predicted to be enhanced by about 275% in nanocrystalline powders.

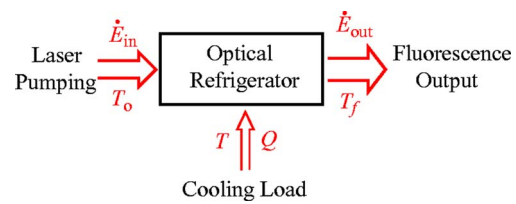The three enhancement methods suggested here for nanopowders can also be applied to bulk materials. The dopant ion concentration can be optimized using the optimum concentration theory developed here; the total pumping energy can be enhanced by placing the sample in an extra- or intracavity; and the optimum phonon DOS and the ion-phonon coupling may be arrived at using alternative host materials. These will be considered in future work.

FIG. 15. (Color online) A control volume showing various energies in and out in the laser cooling of a solid.

APPENDIX A: THERMODYNAMICS LIMIT OF LASER COOLING OF SOLIDS

The theoretical limits of laser cooling are governed by the second law of thermodynamics. An excellent analysis was given by Mungan,[53] in which the ideal cooling efficiency is calculated to be 20%. Here we briefly review the basic concepts and derivation.

A simple control volume is shown in Fig. 15, in which the energy flowing in and out (the pump laser, the external thermal load, and the luminescence emission) are marked. For a narrowband radiation which is independent of the angular directions θ and ϕ over a circular cone of half-angle δ, the energy flux density is given by[53]

$$I_E(\omega) = \frac{1}{4\pi^2}\hbar c^{-2}\bar{f}_{ph}\omega_0^3\,\Delta\omega\sin^2\delta, \qquad (A1)$$

where c is the speed of light, $\bar{f}_{ph}$ is the average photon distribution function over the frequency range, ω_0 is the central frequency, and $\Delta\omega$ is the bandwidth of the beam. The entropy flux density is

$$I_S = \frac{1}{4\pi^2}k_B c^{-2}[(1+\bar{f}_{ph})\ln(1+\bar{f}_{ph}) - \bar{f}_{ph}\ln\bar{f}_{ph}]\omega_0^2\,\Delta\omega\sin^2\delta.$$

$$(A2)$$

It is worth noting what happens if either the bandwidth $\Delta\omega$ or the divergence δ of the source collapses to zero. If its energy flux density is to remain finite, then Eq. (A1) implies that $\bar{f}_{ph}\rightarrow\infty$. In this limit, Eq. (A1) becomes

$$I_S \simeq \frac{1}{4\pi^2} k_B c^{-2} [(1 + \bar{f}_{ph}) \ln \bar{f}_{ph} - \bar{f}_{ph} \ln \bar{f}_{ph}] \omega_0^2 \Delta \omega \sin^2 \delta$$

$$= \frac{k_B}{\hbar \omega} I_{\dot{E}} \frac{\ln \bar{f}_{ph}}{\bar{f}_{ph}} \rightarrow 0, \quad \text{as } \bar{f}_{ph} \rightarrow \infty. \quad \text{(A3)}$$

The entropy carried by monochromatic or unidirectional radiation is zero, so that one can characterize an ideal laser beam as pure work or high-grade energy.

To analyze the limiting efficiency of laser cooling of solids, it is useful to define the flux temperature T_F of the radiation, which is given by

$$T_F \equiv \frac{I_{\dot{E}}}{I_S} = \frac{\hbar \omega_0}{k_B} \frac{\bar{f}_{ph}}{(1 + \bar{f}_{ph}) \ln(1 + \bar{f}_{ph}) - \bar{f}_{ph} \ln \bar{f}_{ph}}. \quad \text{(A4)}$$

Again, for an ideal laser, we have

$$T_F \simeq \frac{\hbar \omega_0}{k_B} \frac{\bar{f}_{ph}}{\ln \bar{f}_{ph}} \rightarrow \infty, \quad \text{as } \bar{f}_{ph} \rightarrow \infty, \quad \text{(A5)}$$

which is consistent with the zero entropy at a finite irradiance. It can be further deduced by Eq. (A5) that the flux temperature of narrow band radiation propagating in a well-defined direction is higher than that of broadband radiation propagating in all directions.

In laser cooling of solids, according to the first law of thermodynamics, we have

$$\dot{E}_{out} = \dot{E}_{in} + Q. \quad \text{(A6)}$$

The cooling coefficient of performance is defined in the usual way for a refrigerator as

$$\eta = \frac{Q}{\dot{E}_{in}}. \quad \text{(A7)}$$

The maximum value of η is the Carnot limit, η_C, and is determined by the second law of thermodynamics. The entropy carried by the fluorescence cannot be less than the sum of the entropy withdrawn from the cooling sample and the entropy transported in by the pump laser, i.e.,

$$\frac{\dot{E}_{out}}{T_f} \geq \frac{\dot{E}_{in}}{T_0} + \frac{Q}{T}, \quad \text{(A8)}$$

where T is the steady-state operating temperature of the refrigerator, and T_f and T_0 are the flux temperatures of the fluorescence and pump radiation, respectively. The reversible Carnot limit is obtained by choosing the equality sign in Eq. (A8). By substituting Eqs. (A6) and (A7) into Eq. (A8), we have

$$\eta_C = \frac{T - \Delta T}{T_f - T}, \quad \text{(A9)}$$

where $\Delta T = T T_f / T_0$.

Consider an example using actual values relevant to laser cooling of Yb^{3+}:ZBLANP.[53] The temperatures of the pump laser and the fluorescence are calculated, using Eq. (A4), to be $T_0 = 7 \times 10^{11}$ K and $T_f = 1760$ K, respectively. Thus the Carnot efficiency of this optical cooler is about 20% at room temperature, and it diminishes approximately linearly to zero as $T \rightarrow 0$. However, the actual cooling efficiency achieved to date is only around 3%, which indicates that much irreversibility has been introduced into the process. One might use a longer pumping wavelength to obtain higher cooling efficiency, but the absorption coefficient of Yb^{3+} would become too small. As a result, the trace impurity absorption will dominate over the Yb^{3+} absorption, and the cooling efficiency η decreases. To reduce these irreversibilities introduced into this process, the sample should be purified to suppress the trace absorption, and also the Yb^{3+} absorption coefficient should be enhanced.

---

*Electronic address: kaviany@umich.edu

[1] P. Pringsheim, Z. Phys. **57**, 739 (1929).

[2] S. Vavilov, J. Phys. (Moscow) **9**, 68 (1945).

[3] S. Vavilov, J. Phys. (Moscow) **10**, 499 (1946).

[4] L. Landau, J. Phys. (Moscow) **10**, 503 (1946).

[5] T. Kushida and J. Geusic, Phys. Rev. Lett. **21**, 1172 (1968).

[6] N. Djeu and W. T. Whitney, Phys. Rev. Lett. **46**, 236 (1981).

[7] R. Epstein, M. Buckwald, B. Edwards, T. Gosnell, and C. Mungan, Nature **377**, 500 (1995).

[8] C. Mungan, M. Buchwald, B. Edwards, R. Epstein, and T. Gosnell, Appl. Phys. Lett. **71**, 1458 (1997).

[9] X. Luo, M. Eisaman, and T. Gosnell, Opt. Lett. **23**, 639 (1998).

[10] B. Edwards, J. Anderson, R. Epstein, G. Mills, and A. Mord, J. Appl. Phys. **86**, 6489 (1999).

[11] T. Gosnell, Opt. Lett. **24**, 1041 (1999).

[12] J. Fernandez, A. Mendioroz, A. J. Garcia, R. Balda, and J. L. Adam, Phys. Rev. B **62**, 3213 (2000).

[13] R. Epstein, J. Brown, B. Edwards, and A. Gibbs, J. Appl. Phys. **90**, 4815 (2001).

[14] A. Rayner, M. Friese, A. Truscott, N. Heckenberg, and H. Rubinsztein-Dunlop, J. Mod. Opt. **48**, 103 (2001).

[15] C. Hoyt, M. Hasselbeck, M. Sheik-Bahae, R. Epstein, S. Greenfield, J. Thiede, J. Distel, and J. Valencia, J. Opt. Soc. Am. B **20**, 1066 (2003).

[16] B. Heeg, M. Stone, A. Khizhnyak, G. Rumbles, G. Mills, and P. Debarber, Phys. Rev. A **70**, 021401(R) (2004).

[17] J. Thiede, J. Distel, S. Greenfield, and R. Epstein, Appl. Phys. Lett. **86**, 154107 (2005).

[18] A. Pires, O. Serra, S. Heer, and H. Gudel, J. Appl. Phys. **98**, 063529 (2005).

[19] M. Hehlen, H. Gudel, Q. Shu, and S. Rand, J. Chem. Phys. **104**, 1232 (1996).

[20] C. Hoyt, in "Laser cooling in thulium-doped solids," Ph.D. thesis, University of New Mexico, Albuquerque, NM, 2003.

[21] B. Heeg, P. Debarber, and G. Rumbles, Appl. Opt. **44**, 3117 (2005).

[22] D. Griffiths, *Introduction to Quantum Mechanics* (Prentice–Hall, Upper Saddle River, NJ, 1995).

[23] W. Hayt and J. Buck, *Engineering Electromagnetics* (McGraw-Hill, Boston, 2001).

[24] E. Zych, Opt. Mater. **16**, 445 (2001).

[25] F. Auzel, J. Lumin. **100**, 125 (2002).

[26] G. Boulon, Y. Guyot, M. Ito, A. Bensalah, C. Goutaudier, G. Panczer, and J. Gacon, Mol. Phys. **102**, 1119 (2004).

[27] R. Powell, *Physics of Solid-State Laser Materials* (Springer-Verlag, New York, 1998).

[28] G. Lei, J. Anderson, M. Buchwald, B. Edwards, R. Epstein, M. Murtagh, and G. Sigel, IEEE J. Quantum Electron. **34**, 1839 (1998).

[29] L. Nurtdinova, V. Semashko, A. Naumov, R. Abdulsabirov, and S. Korableva, Phys. Solid State **47**, 1463 (2005).

[30] S. Rand, Opt. Photonics News **14**, 32 (2003).

[31] D. Wiersma, P. Bartolini, A. Lagendijk, and R. Righini, Nature **390**, 671 (1997).

[32] P. Anderson, Phys. Rev. **109**, 1492 (1958).

[33] X. Ruan and M. Kaviany, Microscale Thermophys. Eng. **9**, 63 (2005).

[34] G. Williams, S. Bayram, S. Rand, T. Hinklin, and R. Laine, Phys. Rev. A **65**, 013807 (2001).

[35] B. Li, G. Williams, S. Rand, T. Hinklin, and R. Laine, Opt. Lett. **27**, 394 (2002).

[36] Z. Zhang and M. Flik, IEEE Trans. Appl. Supercond. **3**, 1604 (1993).

[37] X. Ruan and M. Kaviany, J. Appl. Phys. **97**, 104331 (2005).

[38] B. Heeg, G. Rumbles, A. Khizhnyak, and A. DeBarber, J. Appl. Phys. **91**, 3356 (2002).

[39] C. Kittel, *Introduction to Solid State Physics* (Wiley, New York, 1996).

[40] H. Yang, K. Hong, S. Feofilov, B. Tissue, R. Meltzer, and W. Dennis, J. Lumin. **83-84**, 139 (1999).

[41] C. Loong, P. Vashishta, R. Kalia, W. Jin, M. Degani, D. Hinks, D. Price, J. Jorgensen, B. Dabrowski, A. Mitchell *et al.*, Phys. Rev. B **45**, 8052 (1992).

[42] F. Chou, J. Lukes, X. Liang, K. Takahashi, and C. Tien, Annu. Rev. Heat Transfer **10**, 141 (1999).

[43] M. Paton and E. Maslen, Acta Crystallogr. **19**, 307 (1965).

[44] B. O'Connor and T. Valentine, Acta Crystallogr., Sect. B: Struct. Crystallogr. Cryst. Chem. **B25**, 2140 (1969).

[45] A. Konard, U. Herr, R. Tidecks, F. Kummer, and K. Samwer, J. Appl. Phys. **90**, 3516 (2001).

[46] R. Buckingham, Proc. R. Soc. London, Ser. A **168**, 234 (1938).

[47] G. Lewis and C. Catlow, J. Phys. C **18**, 1149 (1985).

[48] H. Brinkman, W. Briels, and H. Verweij, Chem. Phys. Lett. **247**, 386 (1995).

[49] M. Kilo, R. A. Jackson, and G. Borchardt, Philos. Mag. **83**, 3309 (2003).

[50] A. McGaughey and M. Kaviany, Int. J. Heat Mass Transfer **47**, 1783 (2004).

[51] B. DiBartolo, *Optical Interaction in Solids* (Wiley, New York, 1968).

[52] E. Montoya, F. Agullo-Rueda, S. Manotas, J. G. Sole, and L. Bausa, J. Lumin. **94-95**, 701 (2001).

[53] C. Mungan, Am. J. Phys. **73**, 1458 (2005).